Evaluation of Breast Tumor Detectability With Two Dedicated, Compact Scintillation Cameras

D. P. McElroy, *Student Member, IEEE*, E. J. Hoffman, *Fellow, IEEE*, L. MacDonald, *Member, IEEE*, B. E. Patt, *Member, IEEE*, J. S. Iwanczyk, *Senior Member, IEEE*, Y. Yamaguchi, and C. S. Levin, *Member, IEEE*

***Abstract*—As part of the development of dedicated scintillation cameras for breast imaging, we compared the performances of two dedicated cameras with a standard clinical camera (Siemens Orbiter). One dedicated camera was based on a single position-sensitive photomultiplier tube (PSPMT) coupled to a 6 cm by 6 cm by 6 mm NaI(Tl) crystal. The other (LumaGem) was based on multiple-PSPMTs coupled to a 2 mm $\times$ 2 mm by 6 mm matrix of NaI(Tl) crystals. Spatial resolution was measured with all cameras as a function of depth. The ability of the cameras to image small superficial tumors was tested with a phantom consisting of six hot cylindrical tumors of height 3 mm and varying diameters against a warm background. The tumors were imaged at various depths within the background using tumor-to-background activity concentration ratios of 10 : 1 and 5 : 1. Tumor contrast and signal-to-noise ratio were measured in all cases for all cameras. The dedicated cameras show improved shallow depth of field spatial resolution, contrast, and signal-to-noise ratio relative to the clinical camera when imaging the breast tumor phantom. This, with the additional advantage of being able to position the cameras close to the region of interest, suggests that dedicated cameras will play a strong role in scintimammography and other shallow depth of field applications.**

***Index Terms*—Biomedical nuclear imaging, cancer, image region analysis, object detection, position-sensitive photomultiplier tube (PSPMT), scintillation detectors, scintimammography.**

I. Introduction

ALTHOUGH breast cancer is the most frequently occurring form of cancer in American women, it has a high cure rate if found in its earliest stages (95% five-year survival) [1], [2]. X-ray mammography is the method of choice for detecting early signs of breast cancer because it has a very high diagnostic sensitivity (80%–90%) [1]–[4]. In addition, it is inexpensive and readily available, making it an ideal screening tool. However, X-ray mammography has reduced diagnostic sensitivity in women with dense breasts. It also suffers from poor specificity (10%–35%) [1], [2], [4], particularly for nonpalpable tumors [2], leading to a large number of unnecessary biopsies. In an attempt to reduce this number [5], other imaging modalities, including positron emission tomography (PET), magnetic resonance imaging (MRI), and ultrasound, have tried to address the limitations of mammography and have been used as an adjunct to it in cases where mammograms are inconclusive.

^{99m}Tc-sestamibi (MIBI) is a tracer with high uptake in breast carcinoma compared with normal breast tissue [6]–[9]. Studies using MIBI in single photon planar imaging (scintimammography) have shown high diagnostic sensitivities and specificities in the 80%–95% [7], [10]–[18] range that are essentially independent of breast density. MIBI can also be used to detect lymph-node metastases [8], [9], [19] and may be particularly important in evaluating the sentinel lymph node. MIBI has the advantage of being both relatively inexpensive and more widely available than [^{18}F]2–fluoro-2-deoxy-D-glucose (FDG) PET or MRI, making it an attractive adjunct to mammography in the diagnosis and staging of breast cancer.

Commonly available Anger cameras are not ideal for breast imaging. They are large, bulky, and designed for general-purpose imaging. Breasts are usually imaged in the prone lateral position, so lesions located in the medial quadrants of the breast or near the chest wall may escape detection [18], [20], [21]. Also, due to the limited spatial resolution of these cameras, there is a significant decrease in diagnostic sensitivity for nonpalpable (less than 1 cm diameter) lesions [17]. In response to these problems, we have developed two compact, dedicated scintillation cameras for breast and sentinel node imaging. Small cameras can be tailored to have high intrinsic spatial resolution and high sensitivity. They also are relatively inexpensive. The primary advantage of dedicated gamma cameras for breast imaging is their ability to be positioned on all sides of the breast and to image the breast while under compression. These properties lead to a decreased tumor-to-collimator distance relative to conventional gamma cameras, contributing to improved overall spatial resolution [22], decreased scatter, and, ultimately, improved tumor contrast. Improved spatial resolution contributes to improved lesion contrast recovery by reducing partial volume effects. Scatter is decreased because the amount of scattering material between the source (tumor) and the detector is reduced when the camera is well positioned or the breast compressed [23]. Scatter contributes to decreased lesion contrast recovery by raising the level of the background. Small gamma cameras can also be angled to minimize background radiation from the heart, liver, and other organs, also improving tumor contrast. The dedicated camera is also portable, enabling its use in the mammography suite or in the surgical suite as an aid in locating the sentinel node for biopsy. Potential applications for

Manuscript received November 15, 2000; revised February 1, 2002. This work was supported in part by the California Breast Cancer Research Program under Grant 2TB-0915 K258, by the Department of Energy under Contract DE-FC03-87ER60615, by the National Institutes of Health (NIH) under Grant 5R44CA69988, and by NIH, NCI under #5 R44 CA69988.

D. P. McElroy and E. J. Hoffman are with the Department of Pharmacology, UCLA School of Medicine, Los Angeles, CA 90095-6948 USA (e-mail: dmcelroy@mednet.ucla.edu).

L. MacDonald, B. E. Patt, J. S. Iwanczyk, and Y. Yamaguchi are with Gamma Medica, Division of Photon Imaging, Inc., Northridge, CA 91324 USA.

C. S. Levin is with UCSD/VA Medical Centers, San Diego, CA 92161 USA.

Publisher Item Identifier S 0018-9499(02)06099-9.

use during surgery are numerous, including checking excised areas for residual tumor.

Several groups have been developing small gamma cameras for breast imaging. Many have been based on a single Hamamatsu R3292 5-in-diameter round position-sensitive photomultiplier tube (PSPMT) coupled to both pixilated and slab-type YAP, CsI(Tl), NaI(Tl), or GSO scintillation crystals [24]–[31]. Although intrinsic spatial resolution on the order of 2 mm has been achieved, these round detectors are limited in how close they can be placed to the chest wall. Furthermore, poor energy resolution has characterized detectors based on pixilated scintillation arrays or YAP scintillators due to poor light output. Other groups have developed cameras based on the Hamamatsu 3-in-square series of PSPMTs (R2487 or R3941) coupled to both pixilated or slab'type CsI(Tl) or NaI(Tl) scintillation crystals [32]–[34]. Although similar to our prototype device described below, none have achieved comparable intrinsic spatial resolution. A few groups have reported on the development of detector modules based on the Hamamatsu 1-in^2 series of PSPMTs (R5900-C8) coupled to pixilated scintillator arrays [35]–[38]. We have developed a full field of view (FOV), commercially available gamma camera based on similar detector modules and, to our knowledge, are the first to do so.

In this paper, we evaluate two dedicated scintillation cameras: the first a slab detector prototype device and the other a pixilated device. We compared them to a standard Anger camera by testing their ability to detect artificial breast lesions. Lesions of various sizes are imaged at various depths within a background and scatter environment similar to that expected in a compressed breast. A thorough discussion of small lesion visualization in scintimammography is given in Weinberg *et al.* [39]. We are not trying to quantitatively evaluate image quality in this paper; rather, our goal is to assess whether small, dedicated gamma cameras offer promise as an alternative to the large, multipurpose gamma cameras that are currently in widespread use.

II. Materials and Methods

A. "LumaGem" Dedicated Scintillation Camera

The LumaGem camera (Gamma Medica Inc., Northridge, CA) [40] consists of a compact $15 \times 20 \times 12$ cm^3 head attached to a fully articulating arm that is mounted on a mobile base with onboard electronics and computer for image display and processing. It employs an array of discrete $2 \times 2 \times 6$ mm^3 NaI(Tl) crystals, optically isolated from each other by 0.2 mm of diffuse, optically opaque, reflective material. The pixilated scintillator array is optically coupled through a light guide to an array of 1-in^2 PSPMTs (Hamamatsu Corp., Japan). The PSPMTs are read out via two resistor chains, and the pulses coming out of each of the four ends are amplified and digitized. The total imaging area is approximately 12.5×12.5 cm^2. We tested the camera with a matching square hole collimator (2×2 mm^2 holes, 0.2 mm lead septa, 2 cm thick) and with a hexagonal hole collimator (1.25-mm-diameter holes, 0.25-mm-thick lead septa, 2.4 cm thick). A lead housing to minimize detected radiation from outside the field of view and the housing for each PSPMT result in a minimal 1.25-cm dead area on three sides of the camera head.

The PSPMTs are able to resolve all of the individual scintillator pixels, and a lookup table is created that associates each scintillator pixel with a region on one of the PSPMTs. Events are read in and positioned in a discrete manner within the 2×2 mm^2 area of each crystal. This is in contrast to the continuous positioning and sampling employed in a continuous crystal scintillation camera. Pulse-height spectra are generated for each crystal independently, and the locations of the photopeaks for each crystal are recorded in an energy correction table. This information is used to make an energy window for image acquisition. Finally, the camera is irradiated with a uniform flood source, and the resulting image is used to correct for nonuniformity in sensitivity over the camera's FOV.

B. Prototype Single PSPMT Dedicated Scintillation Camera

A small prototype test camera has previously been reported on by Levin *et al.* [41]–[43] and was evaluated as part of this study. It consists of a single 6 cm $\times$ 6 cm $\times$ 6 mm NaI(Tl) crystal directly coupled with optical grease to a single square Hamamatsu R3941 PSPMT and employs a hexagonal hole collimator (1.5-mm-diameter holes, 0.2-mm lead septa, 2 cm thick). The PSPMT has outer dimensions of 77×77 mm^2 and has a 60×60 mm^2 photocathode active area. The 34 signals from the 16×18 crossed wire anode of the PSPMT are reduced to four through two resistor chains. The four signals are amplified and digitized using CAMAC electronics controlled with a Macintosh running Labview and are saved in list-mode format. The NaI(Tl) crystal has black, light-absorbing material around its sides and white diffuse material on its front (radiation incident) side. The useful field of view with this crystal is about 4×4 cm^2.

Events are positioned in the image matrix in a continuous manner using standard Anger logic. An in-house linearity correction was also developed for this camera that remedies inherent PSPMT nonuniformities and nonlinearities by correctly placing mispositioned events. Other similar corrections have been described in the literature [44]–[47]. We stepped a slit source across the FOV in orthogonal directions and created a slit position map. Comparing this position map with the known actual slit locations, we generate a lookup table of position correction factors, which are applied to the list-mode data postacquisition. In addition, because a PSPMT does not exhibit uniform gain across its FOV, variable energy windowing is performed in a manner similar to that described above for the LumaGem camera.

C. "Orbiter" Multipurpose Scintillation Camera

The Siemens Orbiter (Siemens Medical Systems, Hoffman Estates, IL) is a large general-purpose scintillation camera in routine clinical use in the UCLA nuclear medicine clinic. Measurements were made with this camera using a low-energy high-resolution (LEHR) collimator (2.41 cm thick with 1.13-mm-diameter holes and 0.16-mm lead septa). It employs a 45-cm-diameter 9-mm-thick NaI(Tl) crystal. All linearity, uniformity, and energy corrections are built in to the acquisition system.

D. Spatial Resolution, Energy Resolution, and Sensitivity

Tumor contrast is closely related to system spatial resolution, which has contributions from intrinsic and collimator components. The contribution to system spatial resolution from parallel hole collimators at a distance b from the collimator is given [22] by

$$R = \frac{d(a_e + b + c)}{a_e} \tag{1}$$

where d is the hole width, c is the collimator-to-detector distance, and a_e is the effective hole length. Mather [48] has shown that a_e can be approximated by

$$a_e = a - 2\mu^{-1} \tag{2}$$

where a is the physical hole length and μ is the total linear absorption coefficient.

The spatial resolution was measured for each camera at distances corresponding to the depth of the tumors in background. A line source of ^{99m}Tc was stepped across the FOV and imaged in each position. The positions of the line sources in each image, combined with their known locations, were used to determine the pixel size. The full-width half-maximum (FWHM) of the image profiles then gave the resolution in millimeters. Intrinsic spatial resolution was measured in a similar manner but with the collimator removed and using a 0.5-mm slit in lead irradiated by ^{99m}Tc. All resolution measurements were made near the center of the FOV.

Energy resolution is defined as the FWHM of the (140 keV) photopeak in an energy histogram divided by its energy. Energy resolution was measured for the dedicated cameras by irradiating the FOV with a uniform flood source of activity and creating energy histograms for different regions across the face of the cameras. Energy resolution is important in distinguishing primary events from scattered events, which degrade image contrast.

System sensitivity to incident radiation contributes significantly to the image noise level. High-sensitivity devices can acquire high statistics, low noise images, or images in a shorter length of time compared with low-sensitivity devices. The principal factor in determining system sensitivity is the geometric acceptance, or sensitivity, of the collimator, given [22] by

$$g = \frac{K^2 d^4}{a_e^2 (d+t)^2} \tag{3}$$

where t is the septal thickness and K is constant with the value 0.28 for square holes in a rectangular array and 0.26 for hexagonal holes in a hexagonal array. System sensitivity, defined as counts per second per μCi, was measured by recording the number of counts acquired in a fixed amount of time from a thin, 3-cm-diameter disk of ^{99m}Tc placed on the collimator face. Sensitivity is independent of distance for parallel hole collimators.

E. Tumor Phantom: Contrast and Signal-to-Noise Ratio

An acrylic cylindrical compressed breast tumor phantom of diameter 6 cm and height 1.2 cm, imbedded with six fillable cylinders of height 3 mm and diameters 2, 3, 4, 5, 6, and 7 mm, was designed to be imaged at several depths (distances to the collimator face) within a warm background and scatter environment. In addition, the top of the tumors were cone shaped for ease of filling, with the top of the cone rising about 4 mm above the bottom of each cylindrical tumor. Background and scatter were provided by four cylindrical cavities of inner height 1 cm and outer diameter 6 cm (volume 23 ml). The tumor phantom can be placed in any of five positions within the background. The design simulates a compressed breast. A schematic diagram is shown in Fig. 1.

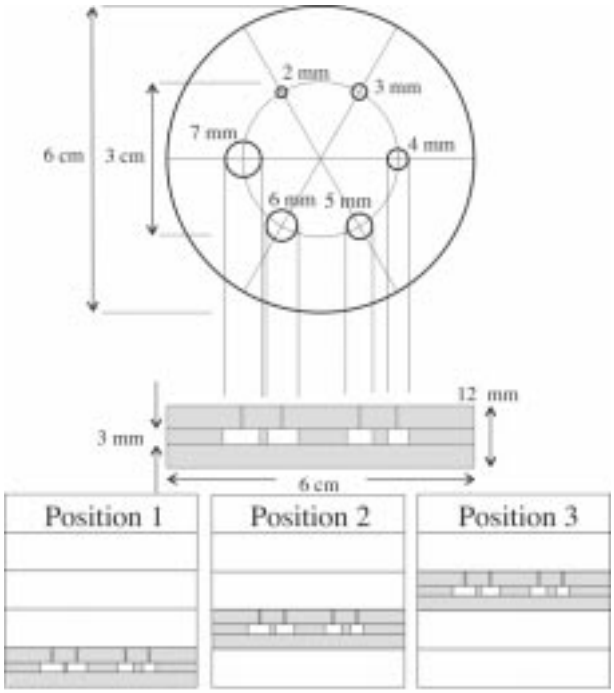

Fig. 1. (Top) Schematic diagram of the cylindrical tumor phantom viewed from the top and the side. (Bottom) The tumor phantom with tumors at distances of 6 mm (position 1), 18 mm (position 2), and 30 mm (position 3) from the collimator face. The collimator would be pictured positioned underneath each image.

The cylindrical tumors and the background cylinders were filled with ^{99m}Tc such that tumor-to-background activity concentration ratios of 10:1 and 5:1 were achieved. This choice was motivated by Maublant *et al.* [9], who reported a (5.64 ± 3.06) : (1.00 ± 0.22) tumor to normal breast tissue ^{99m}Tc-sestamibi uptake ratio for ductal or lobular carcinoma. The tumors were filled with 0.02 or 0.01 mCi/ml, and the background was filled with 0.002 mCi/ml. The tumors were stepped through the background and imaged at each of five positions (Fig. 1), corresponding to tumormCi/mlto-collimator distances of 6, 18, 30, 42, and 54 mm. The phantom was placed directly on the collimator in each case. Images were obtained with LumaGem, the prototype camera, and Orbiter for both activity concentration ratios. One-half of the phantom was imaged at a time with the prototype camera to ensure that the tumors remained sufficiently far from the edge of the FOV. Throughout each series of images, the acquisition time was adjusted to compensate for radioactive decay, with the initial imaging time being 10 min. Thus, the total flux of activity striking the collimators was always constant.

Tumor-to-background contrast in the images was determined by measuring the mean pixel value within a small region of interest (ROI) of constant size placed over each tumor in each image and dividing by the mean background pixel value. The signal-to-noise ratio was also measured for all tumors as the mean pixel value within a small ROI placed over each tumor divided by the standard deviation of the (uniform) background. Where possible, multiple images were taken under identical circumstances, and the tumor contrast measurements were averaged together. All images were processed using a 15% energy acceptance window around the (140 keV) photopeak. The same tumor-to-background activity concentration ratio and the same imaging time was used for all images.

A model was also created that predicts the contrast achievable with an ideal detector. In this case, an ideal detector is defined as being noiseless and having perfect energy resolution. Images were computer generated based on the known activity distribution in the phantom and the known concentration ratios. The 5:1 and 10:1 images were then blurred by applying a Gaussian smoothing kernel with an FWHM equal to the spatial resolution of each camera at each tumor-to-collimator distance. The contrast was measured as the maximum tumor value divided by the mean background value.

III. Results and Discussion

A. Spatial Resolution, Energy Resolution, and Sensitivity

Intrinsic spatial resolution, energy resolution, and sensitivity are shown in Table I for all cameras, along with the collimator dimensions for comparison. Relative to each other, the absolute sensitivity data approximate those expected for each collimator using (3). Sensitivity with the square hole collimator for LumaGem (relative to the hexagonal hole collimator) is increased beyond that expected from the collimator equations alone because the septa lie on top of the gaps between crystals. Intrinsic spatial resolution for LumaGem is equal to the pixel size, as expected. Intrinsic spatial resolution for the Orbiter is worse, as it employs a thicker crystal. The energy resolution quoted for the dedicated cameras is the mean value and standard deviation of all values over the entire FOV. Sample energy spectra from the dedicated cameras are shown in Fig. 2. The orbiter data presented in Table I are from Siemens technical data sheets.

System spatial resolution measurements for all cameras are shown at various distances from the collimator in Fig. 3. Resolution increases approximately linearly with distance from the collimator as expected from (1). The LumaGem camera with the hexagonal hole collimator has the best spatial resolution at all collimator distances, in spite of the fact that the hole size is larger than that of the Orbiter LEHR collimator. This is due to the superior intrinsic resolution of the LumaGem camera. With the 2 mm matching square hole collimator, the resolution of LumaGem is severely degraded. It is comparable with Orbiter at distances close to the collimator face but falls off at larger collimator distances. The prototype camera shows improved resolution compared with Orbiter and similar resolution as the hexagonal hole LumaGem at distances less than 20 mm from the collimator face. Both the prototype and LumaGem

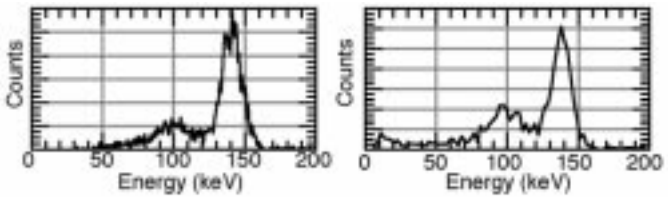

Fig. 2. Sample energy spectra from (a) one region of the prototype camera and (b) one pixel of the LumaGem camera.

TABLE I
INTRINSIC SPATIAL RESOLUTION, ENERGY RESOLUTION, SENSITIVITY, AND COLLIMATOR PROPERTIES FOR ALL CAMERAS IN STUDY AT 140 KEV

	Intrinsic Res. (mm FWHM)	Energy Res. (% FWHM)	Sensitivity (15% Window)	Coll. Thick. (cm)	Hole Dia. (mm)	Septa Thick. (mm)
Prototype	2.2	12.1 ± 3.5	5.9 cps/μCi	2	1.5	0.2
Orbiter	3.6	10.1	3.0 cps/μCi	2.4	1.13	0.16
Hex Luma	2.0	12.2 ± 3.5	1.9 cps/μCi	2.4	1.25	0.25
SQ Luma	2.0	12.2 ± 3.5	7.8 cps/μCi	2	2.0	0.2

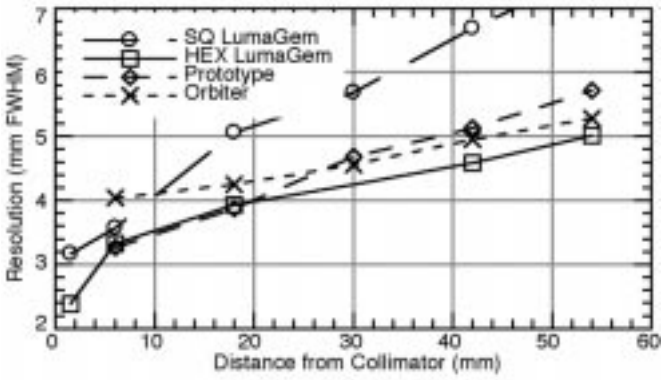

Fig. 3. Overall spatial resolution as a function of distance from the collimator face for the three cameras. Both the square hole and the hexagonal hole collimator are shown for the LumaGem.

with the hexagonal hole collimator show reduced resolution with respect to Orbiter as the distance from the collimator increases.

The observation that spatial resolution decreases with distance from the collimator face at a faster rate for the LumaGem square hole collimator and the prototype camera (2-cm-thick collimators) than it does for Orbiter and the LumaGem hexagonal hole collimator (2.4 cm collimators) is consistent with the fact that their intended use is for shallow depth of field imaging. For a standard compressed breast thickness of 4 to 6 cm, the small cameras should rarely have to image a tumor more than 2 to 3 cm deep in tissue. This, in combination with high intrinsic spatial resolution, allows small gamma cameras to use shorter than standard collimators that, all else being equal, provide increased sensitivity, which is essential for the low-count-rate environment found in Sestamibi breast imaging.

B. Tumor Phantom: Contrast and Signal-to-Noise Ratio

Results of imaging the compressed breast cylindrical tumor phantom at various depths with the three cameras are presented.

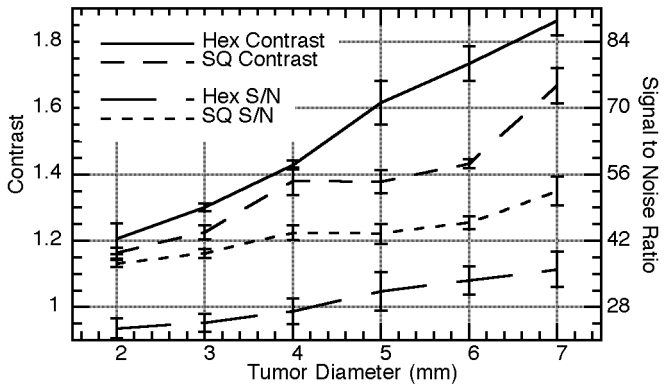

Fig. 4. LumaGem camera contrast and signal-to-noise ratio for two collimators plotted versus tumor diameter for tumors in position 1 (6 mm from the collimator face) with a 10:1 tumor-to-background concentration ratio.

Contrast and signal-to-noise ratio are plotted for a few representative cases as a function of tumor diameter, with error bars representing the standard deviation of three independent measurements. The remainder of the data are presented in tabular form, with error values again representing the standard deviation of three independent measurements. Data are only shown for tumors in positions one through three (3 cm or less from the collimator). Because the average thickness of a compressed breast is 4 to 6 cm (Helvie *et al.* reported a mean compressed breast thickness of 4.4 cm in a study population of 250 mammography patients [49]), dedicated gamma cameras will rarely have to image tumors deeper than 3 cm in tissue. It is worth noting that this study is not entirely realistic, for the tumors are being imaged at equal distances from the collimator with each camera. While this provides a direct comparison of tumor detectability with three cameras, it does not take into account the primary advantage of small scintillation cameras, which is their ability to be positioned close to the region being imaged. While small cameras can easily be maneuvered into positions that minimize the tumor-to-collimator distance, standard gamma cameras are limited in their ability to do this.

Contrast and signal-to-noise ratio are plotted for the LumaGem camera with the tumors at a distance of 6 mm (position 1) from the collimator in Fig. 4. Data are shown for both the small hexagonal hole collimator and for the square hole collimator, with a 10:1 tumor-to-background activity concentration ratio. It is clear from Fig. 4 that using the hexagonal hole collimator results in better tumor contrast but worse signal-to-noise ratio than the square hole collimator for tumors 6 mm from the collimator face. These results coincide with that expected from resolution and sensitivity data. Corresponding contrast values for an ideal detector are plotted in Fig. 5. The remainder of the contrast and signal-to-noise ratio data for the LumaGem camera, for tumors in positions two and three with a 10:1 tumor-to-background ratio, and for tumors in positions one through three with a 5:1 ratio, are presented in Tables II–VI. Similar trends to those in Fig. 4 are seen. The number in parentheses beside the contrast data in the tables represents the fraction of the ideal detector contrast achieved with the measured data, i.e., it is the measured contrast divided by the ideal detector contrast.

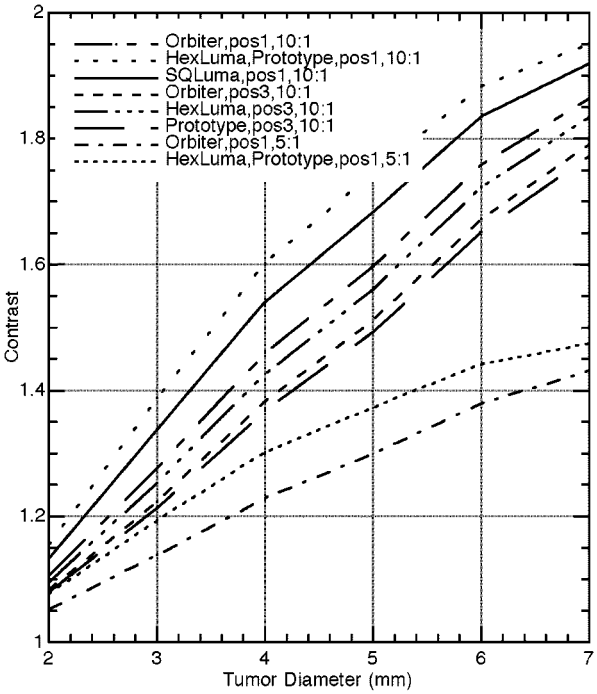

Fig. 5. Tumor contrast as calculated for an ideal detector. Contrast is plotted versus tumor diameter for the three cameras and four collimators with tumors in position 1 (6 mm distance) and position 3 (30 mm distance) and using 5:1 or 10:1 tumor-to-background concentration ratios.

TABLE II
CONTRAST AND SIGNAL-TO-NOISE RATIO FOR LUMAGEM CAMERA WITH SQUARE OR PARALLEL HOLE COLLIMATORS. TUMORS ARE IN POSITION 2 (18 mm FROM COLLIMATOR FACE) WITH A 10:1 ACTIVITY CONCENTRATION RATIO

Dia.	Hex. Contrast	Sq. Contrast	Hex. S/N	Sq. S/N
2 mm	1.16 ± 0.03 (1.04)	1.08 ± 0.02 (1.01)	21.7 ± 0.2	37.1 ± 0.9
3 mm	1.27 ± 0.01 (0.99)	1.13 ± 0.02 (0.95)	24.3 ± 0.2	38.7 ± 1.0
4 mm	1.34 ± 0.06 (0.91)	1.23 ± 0.01 (0.93)	25.3 ± 1.1	42.4 ± 0.9
5 mm	1.49 ± 0.06 (0.92)	1.3 ± 0.04 (0.90)	28.5 ± 1.3	44.0 ± 1.6
6 mm	1.54 ± 0.02 (0.87)	1.31 ± 0.06 (0.82)	29.8 ± 0.2	44.2 ± 2.2
7 mm	1.64 ± 0.05 (0.87)	1.47 ± 0.03 (0.86)	31.8 ± 0.7	50.0 ± 1.4

TABLE III
CONTRAST AND SIGNAL-TO-NOISE RATIO FOR LUMAGEM CAMERA WITH SQUARE OR PARALLEL HOLE COLLIMATORS. TUMORS ARE IN POSITION 3 (30 mm FROM COLLIMATOR FACE) WITH A 10:1 ACTIVITY CONCENTRATION RATIO

Dia.	Hex. Contrast	Sq. Contrast	Hex. S/N	Sq. S/N
2 mm	1.12 ± 0.03 (1.03)	1.01 ± 0.04 (0.95)	21.0 ± 1.7	32.1 ± 4.5
3 mm	1.15 ± 0.03 (0.92)	1.08 ± 0.04 (0.94)	21.5 ± 2.5	33.7 ± 4.7
4 mm	1.28 ± 0.01 (0.90)	1.17 ± 0.03 (0.92)	24.0 ± 2.7	36.6 ± 4.3
5 mm	1.32 ± 0.03 (0.84)	1.21 ± 0.03 (0.89)	24.6 ± 2.4	38.3 ± 5.2
6 mm	1.37 ± 0.01 (0.80)	1.23 ± 0.02 (0.81)	25.7 ± 2.5	38.6 ± 4.0
7 mm	1.48 ± 0.02 (0.81)	1.33 ± 0.03 (0.81)	27.8 ± 2.8	41.5 ± 5.0

These numbers tend to decrease as the tumor diameter increases, indicating that the cameras perform closer to expectation for small diameter tumors. A likely explanation is that for small diameter tumors, the principle decrease in contrast comes as a result of resolution effects, which the tumor model does take into account. For larger diameter tumors, the principle decrease in contrast comes not from resolution effects but from scatter, which the model does not take into account, given that the ideal detector has perfect energy resolution.

TABLE IV
CONTRAST, SIGNAL-TO-NOISE RATIO FOR LUMAGEM CAMERA WITH SQUARE OR PARALLEL HOLE COLLIMATORS. TUMORS ARE IN POSITION 1 (6 mm FROM COLLIMATOR FACE) WITH A 5:1 ACTIVITY CONCENTRATION RATIO

Dia.	Hex. Contrast	Sq. Contrast	Hex. S/N	Sq. S/N
2 mm	1.07 ± 0.02 (1.00)	1.07 ± 0.02 (1.00)	21.4 ± 1.5	55.4
3 mm	1.21 ± 0.06 (1.01)	1.11 ± 0.03 (0.95)	23.5 ± 3.3	57.2
4 mm	1.21 ± 0.07 (0.93)	1.15 ± 0.01 (0.91)	23.0 ± 2.3	60.9
5 mm	1.28 ± 0.03 (0.93)	1.3 ± 0.01 (0.97)	24.6 ± 2.0	68.3
6 mm	1.31 ± 0.04 (0.91)	1.26 (0.89)	25.3 ± 1.8	67
7 mm	1.44 ± 0.01 (0.97)	1.46 ± 0.04 (1.00)	28.5 ± 2.3	75.2

TABLE V
CONTRAST AND SIGNAL-TO-NOISE RATIO FOR LUMAGEM CAMERA WITH SQUARE OR PARALLEL HOLE COLLIMATORS. TUMORS ARE IN POSITION 2 (18 mm FROM COLLIMATOR FACE) WITH A 5:1 ACTIVITY CONCENTRATION RATIO

Dia.	Hex. Contrast	Sq. Contrast	Hex. S/N	Sq. S/N
2 mm	1.1 ± 0.03 (1.04)	—	30.6 ± 2.0	48.2
3 mm	1.16 ± 0.01 (1.01)	1.05 ± 0.01 (0.96)	32.2 ± 2.9	50.1
4 mm	1.22 ± 0.01 (0.98)	1.12 ± 0.02 (0.96)	33.9 ± 2.9	52.8
5 mm	1.25 ± 0.03 (0.96)	1.2 ± 0.03 (0.98)	34.9 ± 4.0	56.1
6 mm	1.29 ± 0.02 (0.93)	1.19 ± 0.03 (0.92)	36.0 ± 3.6	55.9
7 mm	1.34 ± 0.03 (0.93)	1.31 ± 0.03 (0.97)	37.2 ± 2.6	61.4

TABLE VI
CONTRAST AND SIGNAL-TO-NOISE RATIO FOR LUMAGEM CAMERA WITH SQUARE OR PARALLEL HOLE COLLIMATORS. TUMORS ARE IN POSITION 3 (30 mm FROM COLLIMATOR FACE) WITH A 5:1 ACTIVITY CONCENTRATION RATIO

Dia.	Hex. Contrast	Sq. Contrast	Hex. S/N	Sq. S/N
2 mm	—	—	—	—
3 mm	—	—	—	—
4 mm	—	1.08 ± 0.02 (0.95)	—	63.3
5 mm	—	1.14 ± 0.02 (0.96)	—	66.4
6 mm	1.13 ± 0.02 (0.83)	1.14 ± 0.01 (0.91)	29.8 ± 0.7	67.1
7 mm	1.22 ± 0.01 (0.86)	1.23 ± 0.02 (0.93)	32.8 ± 0.8	72.0

Tumor contrast and signal-to-noise ratio for all three cameras are plotted in Figs. 6 and 8 for tumors in positions one and three, respectively, with a 10:1 tumor-to-background ratio. Contrast is plotted in Fig. 10 for tumors in position one with a 5:1 tumor-to-background ratio. Signal-to-noise ratio was left out of Fig. 10, as the trend is very similar to that seen in Figs. 6 and 8. Corresponding contrast values for an ideal detector are plotted in Fig. 5. Corresponding images are shown for the three scenarios, as well as profiles drawn through the 3- and 4-mm-diameter tumors, for subjective evaluation in Figs. 7, 9, and 11. Images acquired with the prototype camera and displayed here are composite images created from the two individual images acquired by imaging half the phantom in each position. The remainder of the contrast and signal-to -noise ratio data, for tumors in position two with a 10:1 tumor-to-background ratio and for tumors in positions two and three with a 5:1 ratio, are presented in Tables VII–IX. Again, the number in parentheses beside the contrast data in the tables represents the fraction of the ideal detector contrast achieved with the measured data, i.e., it is the measured contrast divided by the ideal detector contrast. These numbers again tend to decrease as the tumor diameter increases. Data for the LumaGem camera are not duplicated here.

The tumor-to-background contrast seen with one or both dedicated cameras is greater than or equal to that seen with

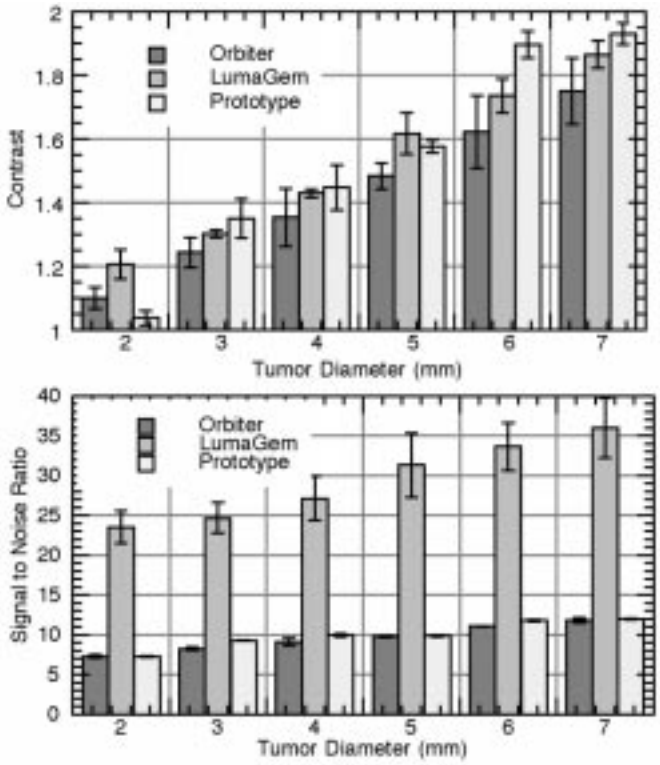

Fig. 6. (Top) Contrast and (bottom) signal-to-noise ratio plotted versus tumor diameter for LumaGem (Hex Hole collimator), prototype, and Orbiter cameras. Tumors are in position 1 (6 mm from the collimator face) and have a 10:1 tumor-to-background concentration ratio.

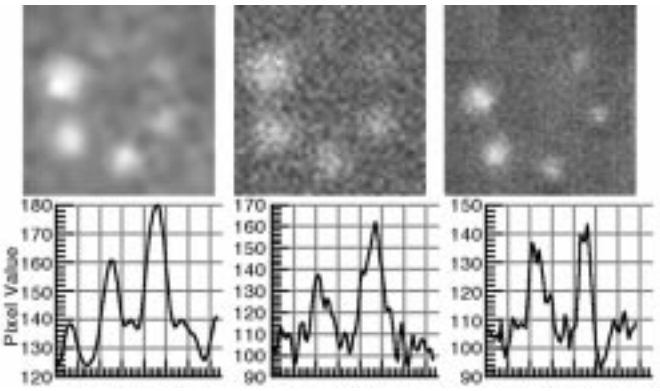

Fig. 7. (Top row) Tumor phantom images for (a) LumaGem, (b) Orbiter, and (c) the prototype camera. Tumors are in position 1 (6 mm from the collimator face) and have a 10:1 tumor-to-background concentration ratio. (Bottom row) Corresponding profiles drawn through the 3- and 4-mm-diameter tumors (right side of each image).

Orbiter at all tumor-to-collimator distances. The difference is not as great, however, for the 5:1 tumor-to-background data. This suggests that imaging tumors with low uptake values may be a weakness of the dedicated cameras. The 2-mm-diameter tumor was not visible in the prototype images. As the prototype camera's resolution is similar to LumaGem at close distances, this may have been due to improper filling of the tumor phantom in this instance. As the distance increases, the smallest tumors are no longer visible as they fall below the resolution limits of the camera and partial volume effects cause them to blur into the background.

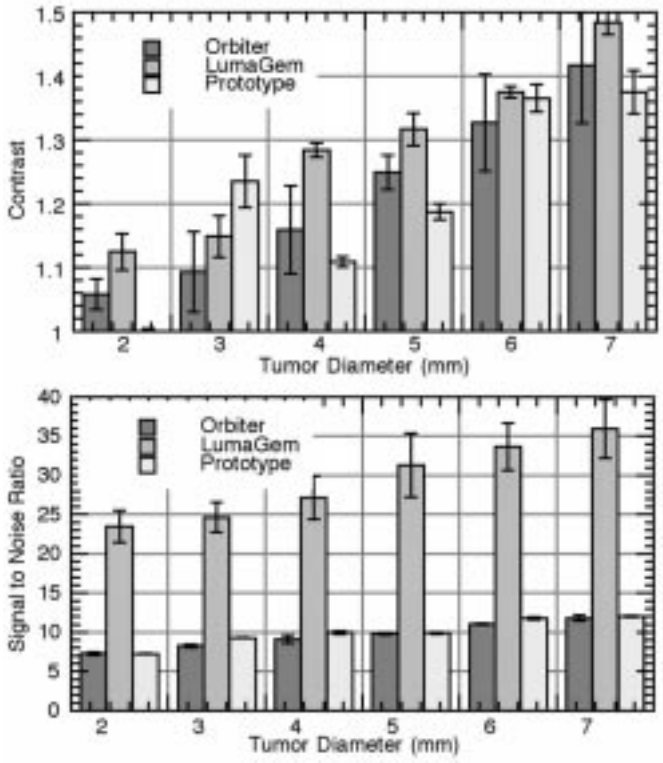

Fig. 8. (Top) Contrast and (bottom) signal-to-noise ratio plotted versus tumor diameter for LumaGem (Hex Hole collimator), prototype, and Orbiter cameras. Tumors are in position 3 (30 mm from the collimator face) and have a 10:1 tumor-to-background concentration ratio.

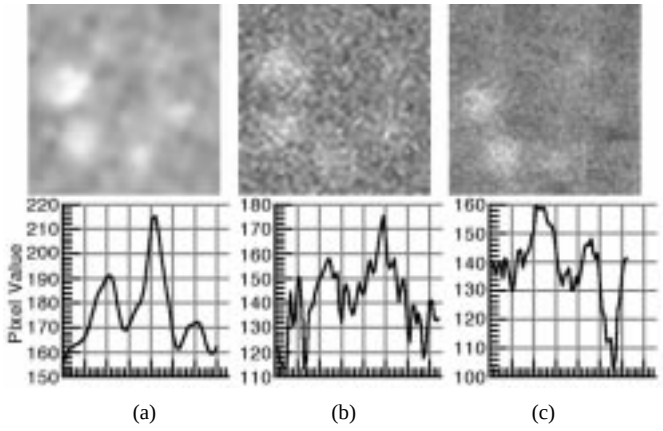

Fig. 9. (Top row) Tumor phantom images for (a) LumaGem, (b) Orbiter, and (c) the prototype camera. Tumors are in position 3 (30 mm from the collimator face) and have a 10:1 tumor-to-background concentration ratio. (Bottom row) Corresponding profiles drawn through the 3- and 4-mm-diameter tumors (right side of each image).

LumaGem clearly had the best signal-to-noise ratio in all cases, in spite of having the lowest sensitivity. One possible explanation is, given that LumaGem is a pixilated system with a relatively small number of pixels, the counts per pixel was far greater. The other two cameras are continuous crystal systems with comparatively larger matrix sizes. In addition, LumaGem employs a flood uniformity correction, creating a very uniform background, whereas the prototype does not. Orbiter and the prototype camera had signal-to-noise values that were similar to each other.

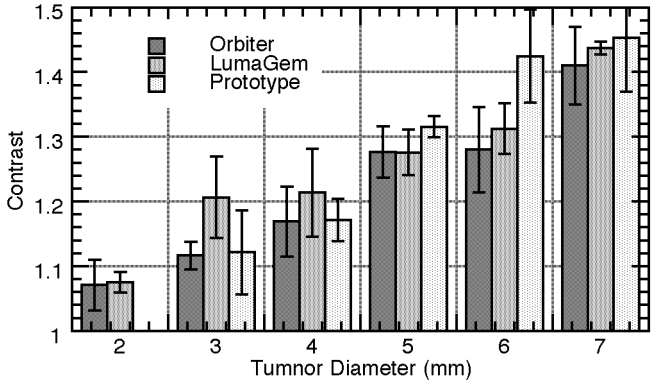

Fig. 10. Contrast plotted versus tumor diameter for LumaGem (Hex Hole collimator), prototype, and Orbiter cameras. Tumors are in position 1 (6 mm from the collimator face) and have a 5:1 tumor-to-background concentration ratio.

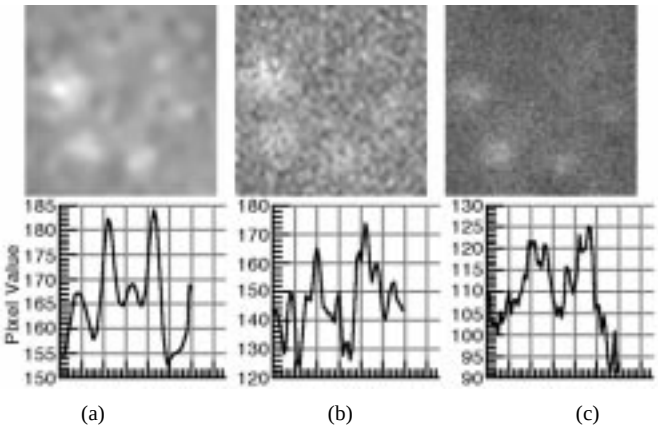

Fig. 11. (Top row) Tumor phantom images for (a) LumaGem, (b) Orbiter, and (c) the prototype camera. Tumors are in position 1 (6 mm from the collimator face) and have a 5:1 tumor-to-background concentration ratio. (Bottom row) Corresponding profiles drawn through the 3- and 4-mm-diameter tumors (right side of each image).

TABLE VII
CONTRAST AND SIGNAL-TO-NOISE RATIO FOR ORBITER AND PROTOTYPE CAMERAS. TUMORS ARE IN POSITION 2 (18 mm FROM COLLIMATOR FACE) WITH A 10:1 ACTIVITY CONCENTRATION RATIO

Dia.	Orbiter Contrast	Prototype Contrast	Orb. S/N	P.T. S/N
2 mm	1.09 ± 0.05 (0.99)	—	6.62	6.5 ± 0.2
3 mm	1.19 ± 0.05 (0.95)	1.25 ± 0.03 (0.96)	7.58	8.3 ± 0.1
4 mm	1.27 ± 0.04 (0.89)	1.21 ± 0.03 (0.82)	8.27	8.1 ± 0.1
5 mm	1.39 ± 0.06 (0.89)	1.34 ± 0.04 (0.83)	8.82	9.2 ± 0.2
6 mm	1.46 ± 0.07 (0.85)	1.62 ± 0.04 (0.91)	9.4	11.2 ± 0.2
7 mm	1.6 ± 0.1 (0.87)	1.62 ± 0.05 (0.86)	10.25	11.1 ± 0.1

TABLE VIII
CONTRAST AND SIGNAL-TO-NOISE RATIO FOR ORBITER AND PROTOTYPE CAMERAS. TUMORS ARE IN POSITION 2 (18 mm FROM COLLIMATOR FACE) WITH A 5:1 ACTIVITY CONCENTRATION RATIO

Dia.	Orbiter Contrast	Prototype Contrast	Orb. S/N	P.T. S/N
2 mm	1.08 ± 0.02 (1.03)	—	7.2 ± 0.4	6.9 ± 0.2
3 mm	1.1 ± 0.06 (0.98)	1.16 ± 0.07 (1.01)	7.6 ± 0.4	8.0 ± 0.2
4 mm	1.08 ± 0.04 (0.89)	1.08 ± 0.07 (0.87)	7.2 ± 0.5	7.5 ± 0.1
5 mm	1.19 ± 0.03 (0.93)	1.12 ± 0.03 (0.86)	7.9 ± 0.1	7.3 ± 0.1
6 mm	1.21 ± 0.05 (0.89)	1.33 ± 0.05 (0.96)	8.0 ± 0.7	8.6 ± 0.2
7 mm	1.29 ± 0.08 (0.91)	1.29 ± 0.09 (0.89)	8.9 ± 0.4	8.1 ± 0.1

TABLE IX
CONTRAST AND SIGNAL-TO-NOISE RATIO FOR ORBITER AND PROTOTYPE CAMERAS. TUMORS ARE IN POSITION 3 (30 mm FROM COLLIMATOR FACE) WITH A 5:1 ACTIVITY CONCENTRATION RATIO

Dia.	Orbiter Contrast	Prototype Contrast	Orb. S/N	P.T. S/N
2 mm	1.02 (0.98)	—	0	6.5
3 mm	1.05 (0.94)	1.06 (0.96)	0	7.5
4 mm	1.03 (0.86)	1.02 ± 0.01 (0.86)	0	7.2 ± 0.1
5 mm	1.14 ± 0.03 (0.90)	1.06 ± 0.01 (0.85)	7.6 ± 0.6	8.0 ± 0.1
6 mm	1.15 ± 0.03 (0.86)	1.22 (0.92)	7.6 ± 0.4	9.3 ± 0.1
7 mm	1.23 ± 0.06 (0.88)	1.2 ± 0.01 (0.86)	8.4 ± 0.8	9.1 ± 0.1

In most cases, tumor signal-to-background ratio tends to be higher for the prototype camera and the LumaGem camera than for the Orbiter. Similarly, the resolution of the small cameras is better than that of Orbiter at distances 30 mm or less from the collimator face. As the tumors are moved farther away from the collimator face, the difference in contrast between the small cameras and Orbiter decreases, roughly following the trend seen in the resolution data.

The tradeoff in medical imaging between resolution and sensitivity is evident when one compares the two LumaGem collimators. The hexagonal hole collimator has clearly better contrast, and the square hole collimator has clearly better signal-to-noise ratio. Both are important in evaluating image quality. Sensitivity is not the only parameter associated with signal-to-noise ratio, however. The superior flood uniformity correction and coarse matrix size of the LumaGem result in tumor signal-to-noise ratios that are clearly better than the other cameras. This is in addition to having better contrast and resolution, resulting in better overall image quality.

IV. CONCLUSION

The two compact, dedicated scintillation cameras we have developed are competitive with commercially available scintillation cameras, particularly in shallow depth of field applications such as breast imaging. Compared with the Siemens Orbiter, they show improved spatial resolution at distances from the collimator that are clinically relevant (30 mm or less), and they have similar or improved sensitivity. As a result, the dedicated cameras produce images that have similar or improved tumor-to-background contrast at tumor-to-collimator distances of 30 mm or less, and they produce images with similar or better tumor signal-to-noise ratios.

One of the primary limitations faced by small gamma cameras is the useful field of view. The prototype camera, for example, has a prohibitively small FOV that even hindered phantom imaging. The FOV of LumaGem, while significantly larger, may nonetheless prove to be near the lower limit of practical size. Further investigation in a clinical situation is necessary to shed more light on this issue.

The primary advantage of small cameras is the ease with which they can be positioned close to the tumor or region of interest where the resolution is highest. In this study, the tumors were equidistant from the collimator for all cameras. This leads us to believe that in a realistic imaging situation, such as in the clinic, the tumor contrast will improve dramatically for the dedicated cameras relative to Orbiter. In addition, we expect the performance of the dedicated cameras to improve with further development. In this paper, we reported on a prototype camera and a camera in its earliest stages of development. The Siemens camera, on the other hand, has had years of research, development, and clinical experience put into its production. This paper indicates that further development, evaluation, and clinical testing of compact, dedicated gamma cameras is warranted, and that they are a feasible alternative to large and bulky clinical gamma cameras.

V. FUTURE WORK

While this paper indicates that dedicated gamma cameras look promising for breast imaging and seem likely to replace general-purpose Anger cameras for application-specific imaging, we acknowledge that evaluating the ability of an imaging system to detect lesions is a complex and highly subjective task. This preliminary work, while not exhaustive, has provided motivation to continue with the development and testing of these cameras. The LumaGem is beginning to undergo clinical trials, and comparative patient studies will be performed. To fully evaluate tumor detectability, a receiver operator characteristics study may have to be performed.

ACKNOWLEDGMENT

The authors would like to thank the technologist staff at the UCLA Nuclear Medicine clinic for their patience and cooperation. They wish to thank Dr. C. Kimme-Smith for her continued support, as well as Dr. S. Cherry, Dr. M. Dahlbom, and Dr. Y. Shao for their valuable input and advice. They would like to acknowledge the help and support of R. Liu, A. Pirogov, E. Tikhomirov, J. Menjivar, M. Damron, A. Ramirez, and P. Lee.

REFERENCES

[1] C. J. Baines, A. B. Miller, C. Wall, D. V. McFarlane, I. S. Simor, R. Jong, B. J. Shapiro, L. Audet, M. Petitclerc, and D. Ouimet-Oliva *et al.*, "Sensitivity and specificity of first screen mammography in the Canadian National Breast Screening Study: A preliminary report from five centers," *Radiol.*, vol. 160, pp. 295–298, 1986.

[2] F. M. Hall, J. M. Storella, D. Z. Silverstone, and G. Wyshak, "Nonpalpable breast lesions: Recommendations for biopsy based on suspicion of carcinoma at mammography," *Radiol.*, vol. 167, pp. 353–358, 1988.

[3] P. O. Hasselgren, R. P. Hummel, D. Georgian-Smith, and M. Fieler, "Breast biopsy with needle localization: Accuracy of specimen x-ray and management of missed lesions," *Surgery*, vol. 114, pp. 836–840, 1993.

[4] T. J. Rissanen, H. P. Mäkärăinen, S. I. Mattila, A. I. Karttunen, H. O. Kiviniemi, M. J. Kallioinen, and O. I. Kaarela, "Wire localized biopsy of breast lesions: A review of 425 cases found in screening or clinical mammography," *Clin. Radiol.*, vol. 47, pp. 14–22, 1993.

[5] D. A. Flanagan, S. B. Gladding, and F. R. Lovell, "Can scintimammography reduce "unnecessary" biopsies?," *Amer. Surg.*, vol. 64, pp. 670–672, 1998.

[6] S. L. Chen, Y. Q. Yin, J. X. Chen, X. G. Sun, Y. Xiu, W. G. Liu, M. Liu, W. M. Zhu, and Y. B. Zhang, "The usefulness of technetium-99m-MIBI scintimammography in diagnosis of breast cancer: Using surgical histopathologic diagnosis as the gold standard," *Anticancer Res.*, vol. 17, pp. 1695–1698, 1997.

[7] J. B. Cwikla, J. R. Buscombe, S. P. Parbhoo, S. M. Kelleher, D. S. Thakrar, J. Hinton, J. Crow, A. Deery, and A. J. Hilson, "Use of 99Tcm-MIBI in the assessment of patients with suspected recurrent breast cancer," *Nucl. Med. Commun.*, vol. 19, pp. 649–655, 1998.

[8] C. H. Kao, S. J. Wang, and S. H. Yeh, "Tc-99m MIBI uptake in breast carcinoma and axillary lymph node metastases," *Clin. Nucl. Med.*, vol. 19, pp. 898–900, 1994.

[9] J. Maublant, M. de Latour, D. Mestas, A. Clemenson, S. Charrier, V. Feillel, G. L. Bouedec, P. Kaufmann, J. Dauplat, and A. Veyre, "Technetium-99m-sestamibi uptake in breast tumor and associated lymph nodes," *J. Nucl. Med.*, vol. 37, pp. 922–925, 1996.

[10] J. R. Buscombe, J. B. Cwikla, D. S. Thakrar, and A. J. Hilson, "Scintigraphic imaging of breast cancer: A review," *Nucl. Med. Commun.*, vol. 18, pp. 698–709, 1997.

[11] J. M. Carril, R. Gómez-Barquín, R. Quirce, O. Tabuenca, I. Uriarte, and A. Montero, "Contribution of 99mTc-MIBI scintimammography to the diagnosis of nonpalpable breast lesions in relation to mammographic probability of malignancy," *Anticancer Res.*, vol. 17, pp. 1677–1681, 1997.

[12] E. J. Clifford and C. Lugo-Zamudio, "Scintimammography in the diagnosis of breast cancer," *Amer. J. Surg.*, vol. 172, pp. 483–486, 1996.

[13] I. Khalkhali, S. Iraniha, J. A. Cutrone, L. E. Diggles, and S. R. Klein, "Scintimammography with Tc-99m sestamibi," *Acta Med. Austriaca*, vol. 24, pp. 46–49, 1997.

[14] I. Khalkhali, S. Iraniha, L. E. Diggles, J. A. Cutrone, and F. S. Mishkin, "Scintimammography: The new role of technetium-99m Sestamibi imaging for the diagnosis of breast carcinoma," *Quart. J. Nucl. Med.*, vol. 41, pp. 231–238, 1997.

[15] S. Mekhmandarov, J. Sandbank, M. Cohen, S. Lelcuk, and E. Lubin, "Technetium-99m-MIBI scintimammography in palpable and nonpalpable breast lesions," *J. Nucl. Med.*, vol. 39, pp. 86–91, 1998.

[16] E. Prats, F. Aisa, M. D. Abós, L. Villavieja, F. García-López, M. J. Asenjo, P. Razola, and J. Banzo, "Mammography and 99mTc-MIBI scintimammography in suspected breast cancer," *J. Nucl. Med.*, vol. 40, pp. 296–301, 1999.

[17] F. Scopinaro, S. Mezi, M. Ierardi, G. De-Vincentis, N. S. Tiberio, V. David, S. Maggi, E. Sallusti, and M. Modesti, "99mTc MIBI prone scintimammography in patients with suspicious breast cancer: Relationship with mammography and tumor size," *Int. J. Oncol.*, vol. 12, pp. 661–664, 1998.

[18] R. Taillefer, A. Robidoux, R. Lambert, S. Turpin, and J. Laperrière, "Technetium-99m-sestamibi prone scintimammography to detect primary breast cancer and axillary lymph node involvement [see comments]," *J. Nucl. Med.*, vol. 36, pp. 1758–1765, 1995.

[19] J. Tolmos, I. Khalkhali, H. Vargas, M. Stuntz, J. Cutrone, F. Mishkin, L. Diggles, R. Venegas, and S. Klein, "Detection of axillary lymph node metastasis of breast carcinoma with technetium-99 m sestamibi scintimammography," *Amer. Surg.*, vol. 63, pp. 850–853, 1997.

[20] I. Khalkhali, L. E. Digles, R. Taillefer, P. R. Vandestreek, P. J. Peller, and H. H. Abdel-Nabi, "Procedure guidelines for breast scintigraphy," *J. Nucl. Med.*, vol. 40, pp. 1233–1235, 1999.

[21] L. Maffioli, R. Agresti, A. Chiti, F. Crippa, M. Gasparini, M. Greco, and E. Bombardieri, "Prone scintimammography in patients with nonpalpable breast lesions," *Anticancer Res.*, vol. 16, pp. 1269–1273, 1996.

[22] H. O. Anger, "Radioisotope Cameras," in *Instrumentation in Nuclear Medicine*, G. J. Hine, Ed. New York: Academic, 1967, vol. 1, pp. 485–552.

[23] R. Pani, F. Scopinaro, R. Pellegrini, A. Soluri, I. N. Weinberg, and G. De Vincentis, "The role of Compton background and breast compression on cancer detection in scintimammography," *Anticancer Res.*, vol. 17, pp. 1645–1649, 1997.

[24] Z. He, A. J. Bird, D. Ramsden, and Y. Meng, "A 5 inch diameter position-sensitive scintillation counter," *IEEE Trans. Nucl. Sci.*, vol. 40, pp. 447–451, Aug. 1993.

[25] C. L. Maini, F. de Notaristefani, A. Tofani, F. Iacopi, R. Sciuto, A. Semprebene, T. Malatesta, F. Vittori, F. Frezza, C. Botti, S. Giunta, and P. G. Natali, "99mTc-MIBI scintimammography using a dedicated nuclear mammograph," *J. Nucl. Med.*, vol. 40, pp. 46–51, 1999.

[26] S. Majewski, B. Kross, L. Majewski, M. Pohl, D. Steinbach, A. G. Weisenberger, R. Wojcik, and A. D. Guerra, "Development of a gamma radiation imaging detector based on a GSO crystal scintillator and a position sensitive PMT," presented at the IEEE NSS and MIC, 1996.

[27] R. Pani, G. De Vincentis, F. Scopinaro, R. Pellegrini, A. Soluri, I. N. Weinberg, A. Pergola, R. Scafe, and G. Trotta, "Dedicated gamma camera for single photon emission mammography (SPEM)," *IEEE Trans. Nucl. Sci.*, vol. 45, pp. 3127–3133, Dec. 1998.

[28] R. Pani, R. Pellegrini, F. Scopinaro, A. Soluri, G. De Vincentis, A. Pergola, F. Iacopi, A. Corona, A. Grammatico, S. Filippi, and P. L. Ballesio, "Scintillating array gamma camera for clinical use," *Nucl. Instrum. Methods A*, vol. 392-1/3, pp. 295–298, 1997.

[29] D. Steinbach, S. Cherry, N. Doshi, A. Goode, B. Kross, S. Majewski, A. G. Weisenberger, M. Williams, and R. Wojcik, "A small scintimammography detector based on a 5″ PSPMT and a crystal scintillator array," presented at the IEEE NSS and MIC, 1997.

[30] M. B. Williams, A. R. Goode, V. Galbis-Reig, S. Majewski, A. G. Weisenberger, and R. Wojcik, "Performance of a PSPMT based detector for scintimammography," *Phys. Med. Biol.*, vol. 45, pp. 781–800, 2000.

[31] R. Wojcik, S. Majewski, B. Kross, D. Steinbach, and A. G. Weisenberger, "High spatial resolution gamma imaging detector based on a 5″ diameter R3292 Hamamatsu PSPMT," *IEEE Trans. Nucl. Sci.*, vol. 45, pp. 487–491, June 1998.

[32] J. N. Aarsvold, R. A. Mintzer, N. J. Yasillo, S. J. Heimsath, T. A. Block, K. L. Matthews, X. Pan, C. Wu, R. N. Beck, and C. T. Chen *et al.*, "A miniature gamma camera," *Ann. New York Acad. Sci.*, vol. 720, pp. 192–205, 1994.

[33] J. H. Kim, Y. Choi, K. S. Joo, B. S. Sihn, J. W. Chong, S. E. Kim, K. H. Lee, Y. S. Choe, and B. T. Kim, "Development of a miniature scintillation camera using an NaI(Tl) scintillator and PSPMT for scintimammography," *Phys. Med. Biol.*, vol. 45, pp. 3481–3488, 2000.

[34] H. K. Seo, Y. Choi, J. H. Kim, K. C. Im, S. K. Woo, Y. S. Choe, K. H. Lee, S. E. Kim, Y. I. Choi, and B. T. Kim, "Performance evaluation of the plate and array types of NaI(Tl), CsI(Tl) and CsI(Na) for small gamma camera using PSPMT," presented at the IEEE NSS and MIC, 2000.

[35] R. Pani, A. Soluri, R. Scafe, A. Pergola, R. Pellegrini, G. De Vincentis, G. Trotta, and F. Scopinaro, "Multi-PSPMT scintillation camera," *IEEE Trans. Nucl. Sci.*, vol. 46, pp. 702–708, June 1999.

[36] R. Pani, A. Pergola, R. Pellegrini, A. Soluri, G. De Vincentis, S. Filippi, G. D. Domenico, A. D. Guerra, and F. Scopinaro, "New generation position-sensitive PMT for nuclear medicine imaging," *Nucl. Instrum. Methods*, vol. 392-1/3, pp. 319–323, 1997.

[37] J. J. Vaquero, J. Seidel, S. Siegel, W. R. Gandler, and M. V. Green, "Performance characteristics of a compact position-sensitive LSO detector module," *IEEE Trans. Med. Imaging*, vol. 17, pp. 967–978, 1998.

[38] J. Seidel, J. J. Vaquero, F. Barbosa, I. Lee, C. Cuevas, W. R. Gandler, and M. V. Green, "Performance characteristics of position-sensitive photomultiplier tubes combined through common X and Y resistive charge dividers," presented at the IEEE NSS and MIC, Seattle, WA, 1999.

[39] I. N. Weinberg, R. Pani, R. Pellegrini, F. Scopinaro, G. DeVincentis, A. Pergola, and A. Soluri, "Small lesion visualization in scintimammography," *IEEE Trans. Nucl. Sci.*, vol. 44, pp. 1398–1402, 1997.

[40] L. MacDonald, B. E. Patt, J. S. Iwanczyk, D. McElroy, and E. J. Hoffman, "LumaGem: High resolution dedicated gamma camera," *J. Nucl. Med.*, vol. 41, pp. 56–56p, 2000.

[41] C. S. Levin, E. J. Hoffman, M. P. Tornai, and L. R. MacDonald, "Design of a small scintillation camera with photodiode readout for imaging malignant breast tumors," *J. Nucl. Med.*, vol. 37, pp. 52–52p, 1996.

[42] ——, "PSPMT and photodiode designs of a small scintillation camera for imaging malignant breast tumors," *IEEE Trans. Nucl. Sci.*, vol. 44, pp. 1513–1520, June 1997.

[43] C. S. Levin, E. J. Hoffman, A. K. Meadors, and M. P. Tornai, "Breast tumor detectability with small scintillation cameras," presented at the IEEE Nuclear Science Symp. Medical Imaging Conf., Albuquerque, NM, 1997.

[44] R. L. Clancy, C. J. Thompson, J. L. Robar, and A. M. Bergman, "A simple technique to increase the linearity and field-of-view in position sensitive photomultiplier tubes," *IEEE Trans. Nucl. Sci.*, vol. 44, pp. 494–498, June 1997.

[45] T. K. Johnson, C. Nelson, and D. L. Kirch, "A new method for the correction of gamma camera nonuniformity due to spatial distortion," *Phys. Med. Biol.*, vol. 41, pp. 2179–2188, 1996.

[46] S. E. King, F. Jih, C. B. Lim, R. Chaney, and E. Gray, "Spectral-spatial-sensitivity distortion trends and an accurate correction method in scintillation gamma cameras," *IEEE Trans. Nucl. Sci.*, vol. NS-32, no. 1, pp. 870–874, 1985.

[47] K. F. Koral, M. E. Schrader, and G. F. Knoll, "A measure of Anger-camera linearity: Results with and without a corrector," *J. Nucl. Med.*, vol. 22, pp. 1069–74, 1981.

[48] R. L. Mather, "Gamma-ray collimator penetration and scattering effects," *J. Appl. Phys.*, vol. 28, no. 1, pp. 1200–1207, 1957.

[49] M. A. Helvie, H. P. Chan, D. D. Adler, and P. G. Boyd, "Breast thickness in routine mammograms: Effect on image quality and radiation dose," *Amer. J. Radiol.*, vol. 163, pp. 1371–1374, 1994.